RSC Advances

PAPER

View Article Online
View Journal | View Issue

Cite this: *RSC Adv.*, 2021, **11**, 32248

$FeNb_2O_6$/reduced graphene oxide composites with intercalation pseudo-capacitance enabling ultrahigh energy density for lithium-ion capacitors†

Shuying Kong,‡*[a] Xu Zhang,‡[b] Binbin Jin,[a] Xiaogang Guo,[a] Guoqing Zhang,[a] Huisheng Huang,[a] Xinzhu Xiang[a] and Kui Cheng*[c]

Received 24th April 2021
Accepted 18th August 2021

DOI: 10.1039/d1ra03198h

rsc.li/rsc-advances

Lithium-ion capacitors (LICs), which combine the characteristics of lithium-ion batteries and supercapacitors, have been well studied recently. Extensive efforts are devoted to developing fast Li^+ insertion/deintercalation anode materials to overcome the discrepancy in kinetics between battery-type anodes and capacitive cathodes. Herein, we design a $FeNb_2O_6$/reduced graphene oxide (FNO/rGO) hybrid material as a fast-charge anode that provides a solution to the aforementioned issue. The synergetic combination of $FeNb_2O_6$, whose unique structure promotes fast electron transport, and highly conductive graphene shortens the Li^+ diffusion pathways and enhances structural stability, leading to excellent electrochemical performance of the FNO/rGO anode, including a high capacity (770 mA h g^{-1} at 0.05 A g^{-1}) and long cycle stability (95.3% capacitance retention after 500 cycles). Furthermore, the FNO/rGO//ACs LIC achieves an ultrahigh energy density of 135.6 W h kg^{-1} (at 2000 W kg^{-1}) with a wide working potential window from 0.01 to 4 V and remarkable cycling performance (88.5% capacity retention after 5000 cycles at 2 A g^{-1}).

1 Introduction

The rapid depletion of fossil fuels, coupled with increasing global demand for sustainable and renewable energy, has stimulated intense exploitation of electrochemical energy storage devices with high energy and power densities.[1,2] Supercapacitors, which feature the advantages of high specific power (>5000 W kg^{-1}), excellent cycling stability (>100 000 times), and high charge–discharge rates, have been studied in depth in recent years.[3] However, their low energy density cannot satisfy the current requirements for large-scale energy storage devices. By contrast, lithium-ion batteries exhibit high energy density with organic electrolyte solutions; however, achieving high power density without affecting their energy density is difficult,[4,5] which has spurred the development of lithium-ion capacitors (LICs).

Many studies have confirmed that LICs combine the energy storage mechanism advantages of lithium-ion batteries and supercapacitors, so these hybrid devices are considered to be one of the most promising energy storage devices.[6,7] The energy storage process of LICs includes both ion absorption/desorption of a capacitive cathode and Li^+ intercalation/deintercalation process of a battery-type anode. The difference in the operating voltage ranges of the two electrodes effectively expands the potential window of LICs, which is advantageous for increasing the energy density.[8–10] Nevertheless, the kinetic imbalance between the capacitive cathode and the battery-type anode of LICs results in remarkable performance deterioration under high-current charge/discharge.[11,12] Consequently, the development of battery-type anode materials with fast Li^+ transmission and high specific capacity for LICs remains a formidable challenge.

Three categories of anode materials that differ by their mechanism have been studied most extensively: alloy-type, conversion-type, and intercalation-type anode materials.[13] Electrode materials that rely on alloying/dealloying and conversion reactions suffer large volume effects, severe polarization, and poor kinetics, resulting in degradation of rate performance and cycle life. By contrast, Li^+ intercalation-type anode materials with fast charge storage ability are considered a reasonable choice for high-performance LICs.[14–17] Titanium-based oxides (*e.g.*, $Li_4Ti_5O_{12}$,[18] TiO_2,[19] TiO_2–B[20]) and niobium-based oxides[21] ($TiNb_2O_7$,[22] T-Nb_2O_5 (ref. 23)) have been extensively researched as intercalation-type anode materials for

[a]*Chongqing Key Laboratory of Inorganic Special Functional Materials, College of Chemistry and Chemical Engineering, Yangtze Normal University, Chong Qing 404100, China. E-mail: kongshuying@126.com*

[b]*School of Materials Science and Engineering, Ningxia Research Center of Silicon Target and Silicon-Carbon Negative Materials Engineering Technology, North Minzu University, Yinchuan 750021, China*

[c]*College of Engineering, Northeast Agricultural University, Harbin 150030, China. E-mail: chengkui@hrbeu.edu.cn*

† Electronic supplementary information (ESI) available. See DOI: 10.1039/d1ra03198h

‡ These authors contributed equally to this work.

nonaqueous LICs. As a typical "zero-strain material", titanium-based oxides, especially $Li_4Ti_5O_{12}$, present excellent rate performance and favorable cycle stability. In addition, their high Li^+ deintercalation potential (~1.55 V *vs.* Li^+/Li) would avoid solid–electrolyte interface (SEI) membrane formation, which is advantageous from a safety standpoint. However, due to the low lithium storage capacity (175 mA h g^{-1}) and poor electronic conductivity (10^{-9} S cm^{-1}) of $Li_4Ti_5O_{12}$, the LICs assembled with it exhibit poor electrochemical performance.[24]

Niobium-based oxides have a high deintercalation lithium potential similar to that of $Li_4Ti_5O_{12}$ (1.2–1.6 V *vs.* Li^+/Li) but a higher specific capacity due to their distinct multivalent-state characteristics. For example, Nb_2O_5 has different electrical pairs (Nb^{5+}/Nb^{4+}, Nb^{4+}/Nb^{3+}) for each Nb atom during the charge/discharge process, corresponding to the insertion and extraction of two Li^+ ions. Thus, the specific capacity of Nb_2O_5 is greater than that of $Li_4Ti_5O_{12}$.[25] Liu *et al.*[26] prepared an orthogonal crystalline Nb_2O_5 nanorod film as an anode material for LICs with excellent performance, achieving a specific capacity of 220 mA h g^{-1} at 1C and an energy density of 95.55 W h kg^{-1} at 5350.9 W kg^{-1}. Currently, some studies have shown that bimetallic niobium-based oxides have better energy storage performance and stability than niobium pentoxide.[27,28] BNb_3O_9 nanobelts prepared by Zhu and co-workers have shown a high reversible capacity of 246 mA h g^{-1} at 100 mA g^{-1}.[29] $Ti_2Nb_{10}O_{29}$ hollow nanofibers prepared *via* a facile co-electrospining technique exhibit a high reversible capacity (307 mA h g^{-1} at 0.1C).[30] Jiao *et al.*[31] reported a novel $TiNb_2O_7$/holey graphene composite material for LICs, with devices exhibiting excellent rate performance (73.5% capacitance retention when current density increased from 0.05 to 5 A g^{-1}).

Here, we used $FeNb_2O_6$/reduced graphene oxide (FNO/rGO) as an insertion-type electrode material for LICs with high energy and power density. The nanocomposite was prepared by anchoring $FeNb_2O_6$ nanoparticles onto rGO nanosheets *via* a simple hydrothermal synthesis method. Combining the orthorhombic columbite $FeNb_2O_6$ nanoparticles with highly conductive graphene not only resulted in fast transmission of ions and electrons but also introduced more electrochemically active sites. The as-synthesized FNO/rGO nanocomposite presents an excellent specific capacity of approximately 770 mA h g^{-1} at a current density of 0.05 A g^{-1} and good cycling stability (95.3% capacitance retention after 500 cycles), as well as much better rate capability than pure FNO anodes. Moreover, a fabricated LIC based on FNO/rGO//ACs exhibited an ultrahigh energy density of 135.6 W h kg^{-1} in the voltage range of 0.01–4 V and stable cycling performance with 88.5% capacity retention over 5000 cycles.

2 Materials and methods

2.1 Synthesis of FNO/rGO

Graphene oxide was prepared using a modified Hummers' method.[32] FNO/rGO was synthesized *via* two hydrothermal reactions expressed as follows:

$$3Nb_2O_5 + 8OH^- \rightarrow [Nb_6O_{19}]^{8-} + 4H_2O \quad (1)$$

$$[Nb_6O_{19}]^{8-} + 8H^+ \rightarrow 3Nb_2O_5 \cdot nH_2O \quad (2)$$

$$Nb_2O_5 \cdot nH_2O + GO\text{–}Fe^{3+} \rightarrow rGO\text{–}FeNb_2O_6\downarrow + nH_2O \quad (3)$$

In detail, as shown as Scheme 1, 0.5 g of Nb_2O_5 and 3 g of KOH were dispersed in a certain amount of DI water with continuous ultrasonic agitation for 2 h to form a dispersed homogeneous solution that was subsequently transferred to a Teflon-lined autoclave and heated at 260 °C for 12 h. The supernatant was then transferred to a beaker, and its pH was adjusted to 7–8 by slow addition of a certain concentration of hydrochloric acid. $FeCl_3$ (molar ratio of $FeCl_3 : Nb_2O_5 = 1 : 1$) was then added and dispersed in the GO solution with ultrasonic assistance. The mixed solution was transferred to a Teflon-lined autoclave and heated at 180 °C for 20 h. The composite was then collected, washed with DI water several times, and dried at 60 °C for 12 h. Finally, the samples were annealed at 600 °C for 2 h under an Ar atmosphere.

For comparison, different concentrations of GO solution (0.2, 0.5, 1, and 2 mg mL^{-1}) were also investigated using the same procedure. The samples were labeled as FNO/rGO-0.2, FNO/rGO-0.5, FNO/rGO-1, and FNO/rGO-2, respectively. In addition, FNO was prepared following the previously described preparation method but without the addition of GO solution.

2.2 Characterization

The morphology of as-prepared samples was investigated using transmission electron microscopy (TEM, Jeol 2100F) and scanning electron microscopy (SEM, JSM-7001F) in conjunction with energy-dispersive X-ray spectroscopy (EDS). The crystal structure of the as-prepared materials was determined *via* X-ray diffraction (XRD) analysis using a diffractometer (Ultima IV) equipped with a Cu Kα radiation source ($\lambda = 0.15$ nm). The surface composition and chemical state were characterized by X-ray photoelectron spectroscopy (XPS, Thermo ESCALAB 250XI). The Raman spectra of products were obtained with a Renishaw inVia Raman microscope with an excitation wavelength of 532 nm. Thermogravimetric analysis was carried out with a Netzsch STA 449 F388 thermal analysis system.

2.3 Electrochemical characterization

The electrochemical performances of the FNO/rGO composite materials were tested with CR2032 coin cells, which were fabricated in an Ar-filled glove box. For fabrication of working electrodes, 80 wt% of FNO/rGO active material, 10 wt% of acetylene black, and 10 wt% of polyvinylidene fluoride in *N*-methyl-2-pyrrolidone were well mixed and coated onto copper foil. The coated sheet was then dried in a vacuum oven at 80 °C for 12 h and cut into circular electrodes with a diameter of 12 mm. The electrolyte was 1 M $LiPF_6$ in dimethyl carbonate, ethylene carbonate and diethyl carbonate (1 : 1 : 1, in volume percent). The full cell of LICs was fabricated with an FNO/rGO anode and an AC cathode, the anode-to-cathode mass ratio being 5. The fabricated half-cells contained the working electrode, lithium metal as the counter and reference electrodes with the same electrolyte.

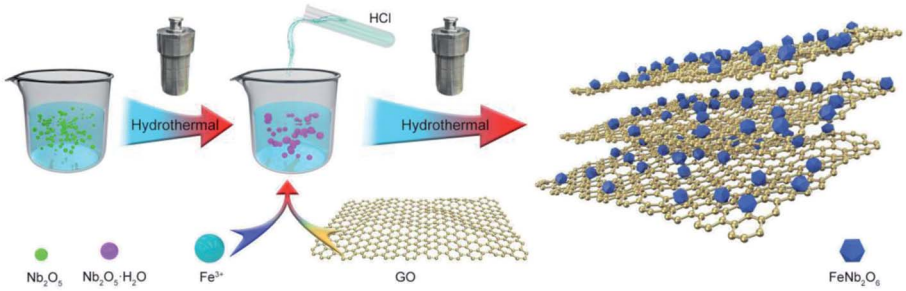

Scheme 1 Schematic illustration of the process for fabricating FNO/rGO composite.

Cyclic voltammetry (CV) was carried out with an electrochemistry workstation (CH Instruments CHI660E) in the potential window from 0.01 to 3.0 V for the FNO/rGO anode. Galvanostatic charge–discharge (GCD) experiments were conducted within the potential window from 0.01 to 3.0 V with a battery test instrument (Land CT2001). CV and GCD experiments with the LICs were performed between 0.01 and 4 V.

The power density P (W kg^{-1}) and energy density E (W h kg^{-1}) of the LICs were calculated according to the following equations:[33]

$$P = \frac{E}{\Delta t} \times 3600 \quad (4)$$

$$E = \frac{1}{2} C_m \times \Delta V^2 \times \frac{1}{3.6} \quad (5)$$

where Δt (s) is the discharge time, ΔV (V) is the discharge voltage range, and C_m (F g^{-1}) is the specific capacitance of the LICs.

3 Results and discussion

Fig. 1a shows a model of the crystal structure of the columbite FNO. The columbite crystal structure comprises a slightly distorted hexagonal close-packed (hcp) oxygen sublattice along the *a*-axis layers. Fe and Nb are located at the 4c and 8d sites with six surrounding oxygen atoms. The formed FeO_6 and NbO_6 octahedra are connected by sharing edges and angles and are arranged in a zigzag pattern along the *c*-axis. These parallel FeO_6 and NbO_6 layers are arranged in an alternating Fe–Nb–Nb–Fe–Nb–Fe sequence along the *a*-axis.[34] The unique crystalline structure of FNO is advantageous to the transmission and diffusion of Li^+, suggesting that it can be used as a LIC anode material with enhanced kinetics. However, FNO exhibits poor electrical conductivity, which is a common shortcoming among metal oxides. Thus, we used graphene as a conducting medium for FNO due to its outstanding electronic conductivity and large theoretical surface area. The synergetic effects between FNO and rGO can provide more electrochemically active sites and facilitate the infiltration of the electrolyte such that the electrochemical reaction kinetics, specific capacity, electrical conductivity, and cycle life of the material will be substantially improved.

As shown in Fig. 1b, the XRD pattern of the rGO sample presents two diffraction peaks appearing at 25° and 43°, corresponding to the (002) and (100) planes of graphite, respectively (JCPDS no. 65-6212). After FNO was anchored onto the surface of rGO, the intensity of the graphitic peaks decreased. The peaks at 24.2°, 30.1°, 35.5°, 47.9°, 53.1°, 60.4°, and 64.1° in the pattern of the FNO/rGO composite are attributed to the (111), (131), (002), (202), (261), (133), and (203) planes, respectively, which index well with the standard orthogonal $FeNb_2O_6$ phase (JCPDS no. 34-0426). The structures of the rGO and FNO/rGO were further investigated by using Raman spectroscopy, as shown in Fig. 1c. The two dominant feature peaks of rGO and FNO/rGO are the D band at 1358 cm^{-1} and the G band at 1568 cm^{-1}.[35] The I_D/I_G ratio is a key parameter indicating the degree of disorder in graphitic materials. The I_D/I_G ratio decreased after FNO was added (1.02 for rGO and 0.97 for FNO/rGO), which suggests that the amorphous carbon was partially converted to crystalline carbon in the presence of FNO. The Raman spectrum of FNO/rGO shows additional peaks at 865, 631, 523, and 472 cm^{-1}, corresponding to Nb–O lattice vibrations.[36] In addition, peaks are located below 400 cm^{-1}, corresponding to Fe–O or O–Nb–O bonds.[37,38]

The surface chemical composition of FNO/rGO was characterized *via* XPS analyses. Fig. 1d shows the wide-scan XPS spectrum of the composite, which confirms the presence of C, O, Nb, and Fe element species without impurities. The high-resolution Nb 3d spectrum is presented in Fig. 1e. The peaks at 206.7 eV and 209.3 eV are ascribed to Nb $3d_{5/2}$ and Nb $3d_{3/2}$, respectively. According to the spin–orbit separation of Nb 3d, the ΔE of 2.6 eV indicates that the valence of Nb in the sample is Nb^{5+}. The characteristic peak for C 1s was divided into three peaks (Fig. S1†) at 284.8, 285.3, and 286.0 eV, corresponding to C=C, C–C, and C–O, respectively. The Fe 2p spectrum is shown in Fig. 2f. The major peaks at 710.8 eV and 724.4 eV correspond to Fe $2p_{3/2}$ and Fe $2p_{1/2}$.[39]

The microstructural morphologies of the FNO/rGO composites were revealed by SEM and TEM. Fig. 2a–e display the SEM images of the FNO/rGO composites synthesized with different concentrations of GO solution. Fig. 2a showing the FNO sample without rGO presents a uniform particle morphology with slight agglomeration. When graphene is introduced, the FNO particles are scattered and the agglomeration is slightly reduced (Fig. 2b–e). By contrast, when the concentration of GO solution is 0.5 mg mL^{-1}, the FNO nanoparticles are anchored onto the surface of the graphene without obvious aggregation. Moreover, the uniform FNO nanoparticles

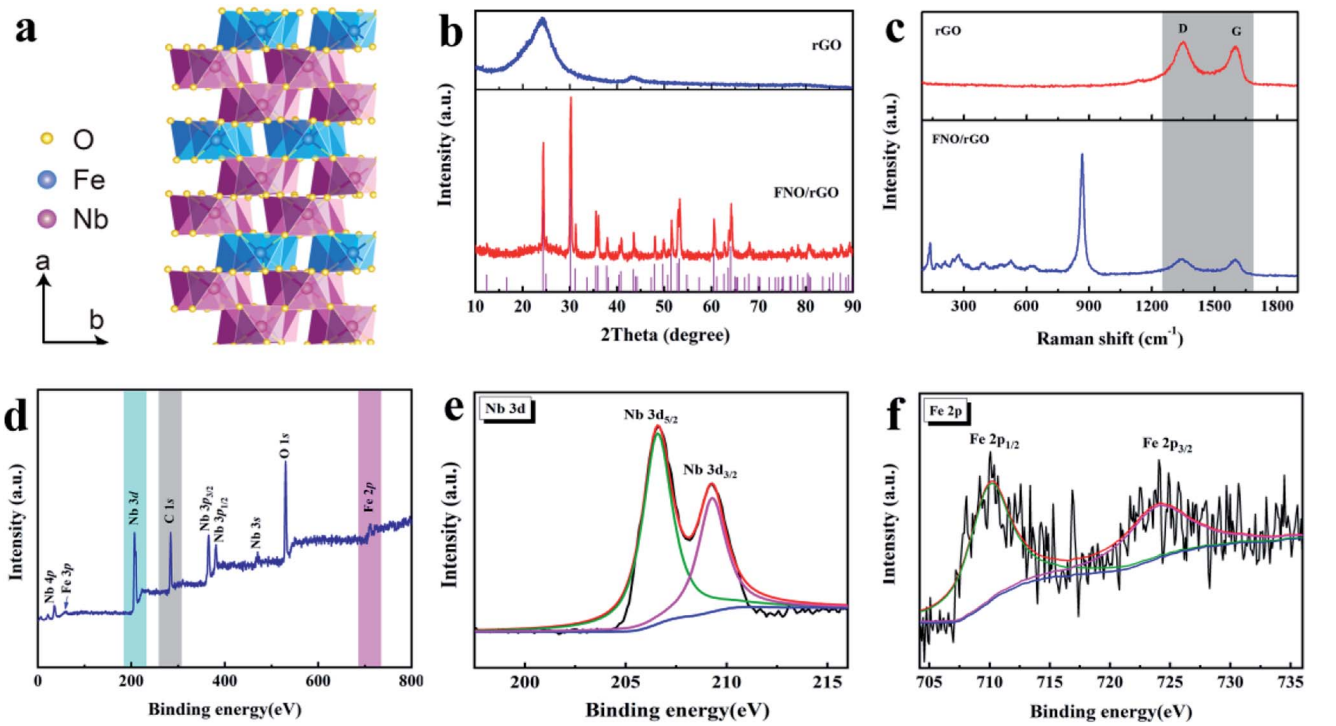

Fig. 1 (a) The crystal structure of columbite FNO. (b) XRD patterns and (c) Raman spectra of rGO and the FNO/rGO composite. (d) The wide-scan XPS survey spectrum, (e) Nb 3d spectrum, and (f) Fe 2p spectrum of the FNO/rGO composite.

occupy gaps between the graphene nanosheets, preventing graphene from stacking, further shortening the ion diffusion distance and enhancing the utilization of active materials.

The SEM image with corresponding EDS element mapping images are shown in Fig. 2f, unambiguously confirming that the FNO nanoparticles are evenly distributed throughout the graphene surface. TEM images of FNO/rGO show that the particle size of FNO is approximately 80–120 nm and that the particles are supported homogeneously on ultrathin graphene nanosheets (Fig. 2g and h). Fig. 2i shows a HRTEM image of FNO, which clearly reveals lattice spacings of 0.172 nm, 0.296 nm, and 0.336 nm, corresponding to the (261), (131), and (111) planes of FNO, respectively. In addition, the lattice fringes are continuous, indicating that the as-prepared FNO nanoparticles are highly crystalline. Moreover, graphene is clearly observed in the HRTEM image, further confirming that graphene was attached to the FNO nanoparticles.

To investigate the electrochemical performances of the pure FNO and FNO/rGO prepared with different concentrations of GO, half-cells were assembled and measured within the potential range from 0.01 to 3.0 V. The Li storage performance of the FNO/rGO anodes prepared with different concentrations of GO was studied by GCD at 0.05 A g^{-1} from 0.01 to 3.0 V (Fig. S2†). As shown, compared with the pure FNO electrode, the FNO/rGO anode shows superior electrochemical performance, suggesting synergetic effects between FNO and rGO. Moreover, the FNO/rGO-0.5 electrode exhibited the longest discharge time. The reversible capacity of the FNO/rGO-0.5 electrode is 770 mA h g^{-1} at a current density of 0.05 A g^{-1}, which is much larger than the reversible capacities of FNO/rGO-0.2 (541.9 mA h g^{-1}), FNO/rGO-1 (603 mA h g^{-1}), FNO/rGO-2 (506.4 mA h g^{-1}), and FNO (470 mA h g^{-1}).

Fig. 3b displays the rate performance of the FNO/rGO composites prepared with different concentrations of GO. The FNO/rGO-0.5 electrode achieved reversible capacities of 770, 698, 650.3, 571, 502, 452.7 mA h g^{-1} at current densities of 0.05, 0.1, 0.2, 0.5, 1, and 2 A g^{-1}, respectively. The reversible capacity retention returned to 702 mA h g^{-1} when the current density went back to 0.05 A g^{-1}, suggesting superior rate capability. By contrast, the rate performance of FNO/rGO-0.5 is much better than those of the other FNO/rGO composites (77.3% for FNO/rGO-0.2, 85.9% for FNO/rGO-1, 73% for FNO/rGO-2, and 71% for FNO). Notably, the presence of a certain amount of rGO improved the conductivity, charge transfer speed, and electrochemical kinetics of the material. However, the aggregation and restacking of excess rGO would restrain ion transport at the electrochemical interfaces and then cause greater loss of reversible capacity of the electrodes. The Nyquist plots of the FNO/rGO composites prepared with different concentrations of GO are exhibited in Fig. S3.† After simulation, the values of the charge transfer resistance (R_{ct}) for FNO/rGO-0.2, FNO/rGO-0.5, FNO/rGO-1, FNO/rGO-2, and FNO electrodes are 38.8 Ω, 34.7 Ω, 40.0 Ω, 44.6 Ω, and 60.4 Ω, respectively. Obviously, the presence of rGO could increase the electrical conductivity and decrease the charge transfer resistance. Moreover, the FNO/rGO-0.5 electrode has the lowest R_{ct}, which benefits the rate capability. The corresponding lithium ion diffusion coefficient (D_{Li}) was calculated from the following equations:

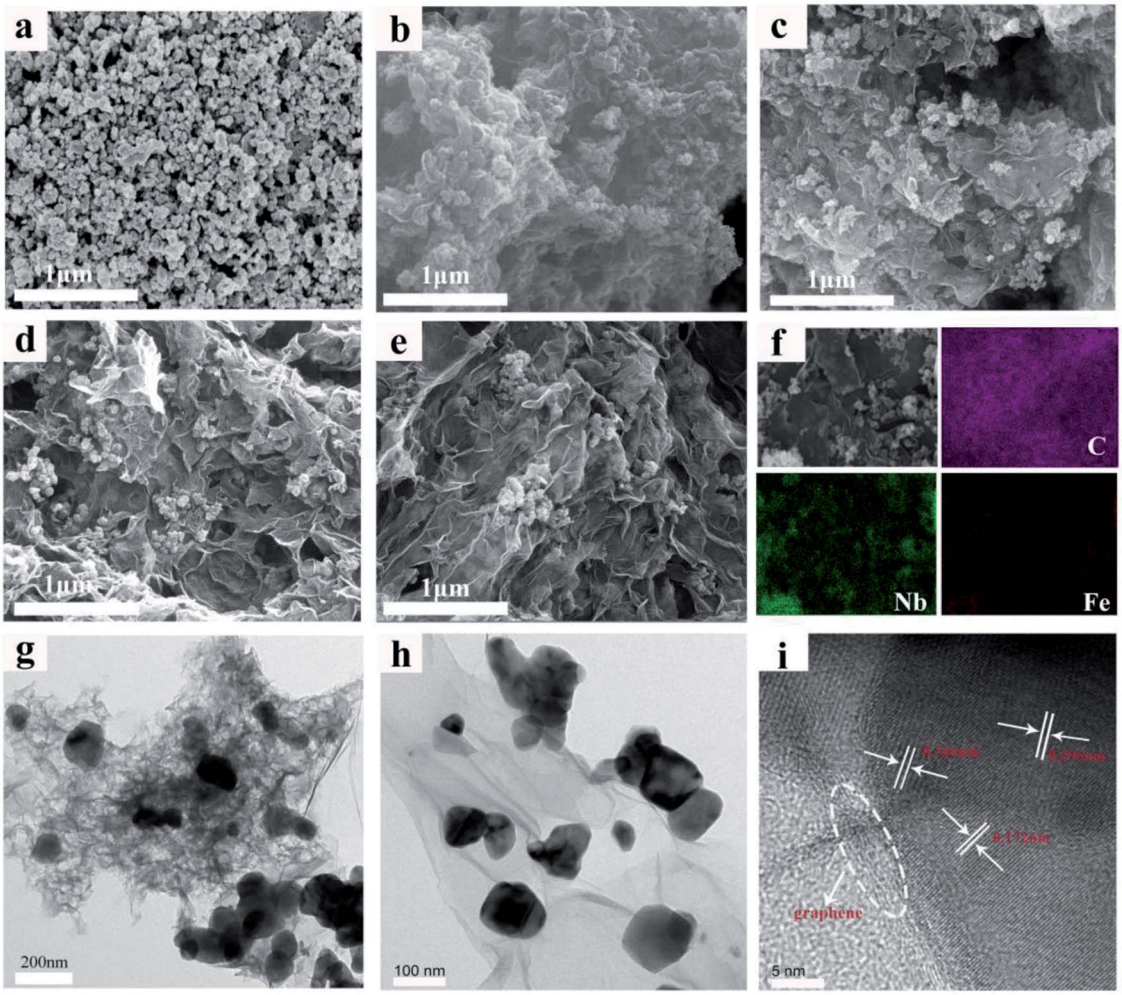

Fig. 2 (a–e) SEM images of the FNO/rGO composites synthesized with different concentrations of GO solution ((a): FNO; (b): FNO/rGO-0.2; (c): FNO/rGO-0.5; (d): FNO/rGO-1; (e): FNO/rGO-2). (f) SEM image with corresponding EDS element mapping images. (g and h) TEM and (i) HRTEM (high-resolution TEM) images of the FNO/rGO-0.5 composite.

$$D = R^2T^2/2A^2 2n^4F^4C^2{\sigma_W}^2 \quad (6)$$

$$Z = R_e + R_{ct} + \sigma_W\omega^{-1/2} \quad (7)$$

where R is the gas constant, T is the absolute temperature, A is the surface area of the electrode, n is the number of electrons transferred in the redox reaction, F is the Faraday constant, C is the concentration of lithium ions, and σ_W is the Warburg factor, which can be calculated from the slope of the line between Z' and $\omega^{-1/2}$. The values of σ_W of the FNO/rGO-0.2, FNO/rGO-0.5, FNO/rGO-1, FNO/rGO-2, and FNO electrodes are calculated as 5.46, 4.17, 6.89, 8.23, and 8.84 ($\Omega\ s^{-1/2}$), respectively (Fig. S4†). Obviously, the lithium ion diffusion coefficient of FNO/rGO is higher than that of LTO; therefore, the addition of graphene can effectively enhance the kinetics of lithium ion transfer.

Fig. 3c shows the first four cycles of the CV curve of the FNO/rGO-0.5 electrode in the potential range 0.01–3 V at 0.5 mV s^{-1}. A spiky peak (~0.62 V) is observed in the first cycle, which is attributed to the insertion of Li^+ ions and the formation of an SEI. Except for the CV curve corresponding to the first cycle, the CV curves overlap almost perfectly with each other, which indicates good reversibility and cycling stability. In the second cycle, several cathode/anode peaks at ~1.5/1.85 V are attributed to the reversible reaction of Nb^{4+}/Nb^{5+}. Moreover, a broad hump between 0.8 V and 1.5 V is assigned to the Nb^{3+}/Nb^{4+} redox couple.[40] Fig. 3d shows the GCD curves for the first four cycles of the FNO/rGO-0.5 composite. The capacity at the first cycle is much higher than those at subsequent cycles, which is mostly caused by the formation of an SEI. Moreover, the regions with sloping voltage plateaus are consistent with the CV results. The CV curves of the FNO/rGO-0.5 electrode at sweep rates from 0.01 to 3 V are shown in Fig. 3e. A slight potential separation was observed with increasing sweep rate because of the excellent reversibility and fast lithium-ion insertion/extraction processes. Through the thermogravimetric test of FNO/rGO-0.5 in air, the mass fraction of graphene can be determined as 12.1% (Fig. S5†).

The relationship between the peak current (i) and the sweep rate (v) is based on the following equation:[41]

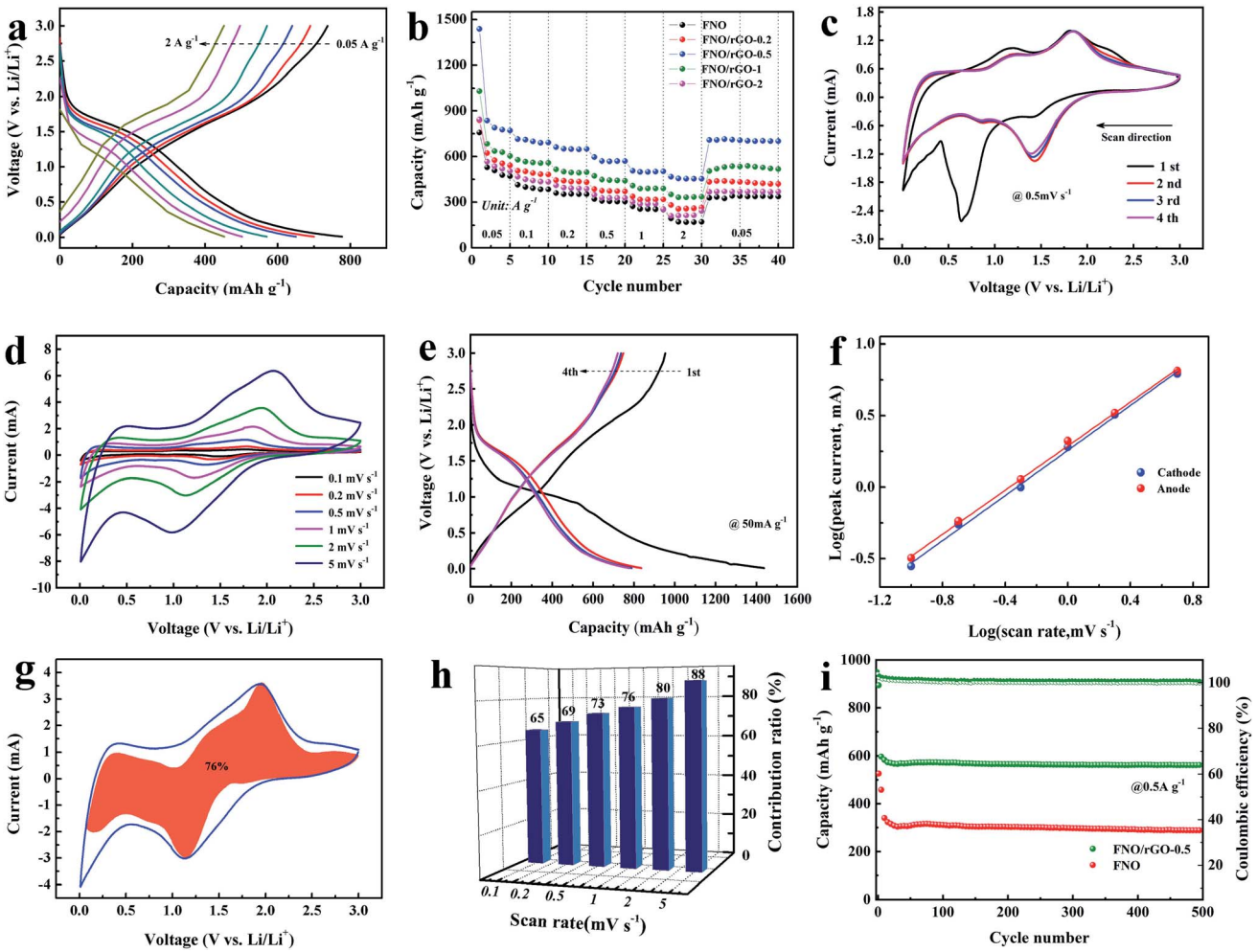

Fig. 3 (a) GCD curves of FNO/rGO-0.5 at different current densities. (b) The rate performance of the FNO/rGO composites prepared with different concentrations of GO. (c) CV curves at a scan rate of 0.5 mV s^{-1} of FNO/rGO-0.5. (d) GCD curves of FNO/rGO-0.5 at a current density of 50 mA g^{-1}. (e) CV curves at different scan rates of FNO/rGO-0.5. (f) The *b* value of specific peak currents with different scan rates. (g) CV curves of FNO/rGO-0.5 with separation between total current and capacitive current (shaded region) at 1 mV s^{-1}. (h) Capacitive contributions of FNO/rGO-0.5 at various scan rates. (i) Cycling performance at 0.5 A g^{-1}.

$$i = av^b \quad (8)$$

where *a* and *b* are adjustable parameters. In eqn (8), the *b* values can be used to judge the charge storage mechanism of the materials, which is a diffusion-controlled process ($b = 0.5$) or a capacitive-controlled process ($b = 1$) *via* a surface faradaic redox reaction.[42] The log(*i*) *versus* log(*v*) plots of the FNO/rGO-0.5 composite are presented in Fig. 3f. The *b* values of the anodic peak and cathodic peak are 0.77 and 0.79, confirming the surface-controlled capacitive behavior of the FNO/rGO-0.5 material. Thus, the major charge storage mechanism of FNO/rGO-0.5 is beneficial to fast charge transfer, resulting in excellent rate capability and cycle performance. Furthermore, the ratios of the diffusion-controlled and capacitive-controlled processes were analyzed by the method by Dunn *et al.*:[43]

$$i(\mathrm{V}) = k_1 v + k_2 v^{1/2} \quad (9)$$

where $i(\mathrm{V})$ is the current corresponding to a fixed potential, v is the scan rate, and k_1 and k_2 are constants. Fig. 3g shows that the capacitive contribution is 76%, which is compared with the total measured charge at a sweep rate of 1 mV s^{-1}. The ratios of capacitive contribution under the different scan rates are shown in Fig. 3h, which increase gradually with increasing scan rate. The cycling stability of FNO/rGO-0.5 and FNO is shown in Fig. 3i. FNO/rGO-0.5 exhibited excellent cycle performance, which shows 95.3% capacitance retention after 500 cycles at a charge/discharge current density of 0.5 A g^{-1} with a coulombic efficiency of 99.6%, suggesting a much higher capacitance retention than FNO (88%). In order to further explore the morphology and structure of the FNO/rGO-0.5 electrode after long-term cycling, SEM, XRD and XPS analyses of the FNO/rGO-0.5 electrode have been performed. As shown in Fig. S6,† the FNO particles are still retained after the cycling, and the particles and graphene nanosheets agglomerate slightly due to the presence of the binder. The structure of the FNO/rGO-0.5

electrode after the cycling was investigated and the results are shown in Fig. S7 (XRD) and S8 (XPS).† The XRD characterization shows that the diffraction peaks of FNO after the cycling are weaker than for fresh FNO, which is due to the insertion and extraction of Li^+ ions. As shown in Fig. S8,† the XPS test results are consistent with the XRD results. The peak strength of Nb 3d and Fe 2p decreases; moreover, the characteristic peak for C 1s becomes stronger, which could be due to the presence of conductive carbon.

In order to further explore the lithium storage mechanism of the FNO material, *ex situ* XRD patterns corresponding to first charge/discharge cycle are exhibited in Fig. 4. The peaks appearing at 24.2°, 30.1°, 35.5°, 47.9°, 53.1°, 60.4°, and 64.1° are attributed to the (111), (131), (002), (202), (261), (133), and (203) planes of fresh FNO (JCPDS no. 34-0426), respectively. As shown in Fig. 4b, during the discharge process from state a to c, the peaks shift to lower bonding energy. And then during the charge process from state c to d, they nearly recover to the angles of the fresh sample. This phenomenon suggests that the lattice undergoes shrinkage and enlargement, which results from the insertion and extraction of Li^+ ions.

The LIC was assembled using FNO/rGO-0.5 as the anode and ACs as the cathode, as shown in Fig. 5a. The highest voltage attained was 4.0 V, which may lead to high energy and power densities. When the LIC system is charged, Li^+ ions rapidly intercalate into the FNO/rGO anode; meanwhile PF_6^- ions adsorb onto the AC cathode/electrolyte interface to form double layers. Fig. 5b exhibits CV curves of the FNO/rGO//ACs LIC, as recorded at different sweep rates in the voltage range from 0.01 to 4 V. The shape of the CV curves is not strictly rectangular, which is attributed to a combination of two different energy storage mechanisms with Li^+ intercalation/deintercalation process and anion adsorption/desorption process. A similar shape was maintained even at a high scan rate of 100 mV s^{-1}, revealing remarkable rate capability and rapid energy storage kinetics. Fig. 5c shows the GCD curves of the FNO/rGO//ACs LIC at different current densities. These curves differ from a near–linear correlation of ideal supercapacitor properties, revealing the two energy storage mechanisms of the FNO/rGO//ACs LIC. After calculating specific capacitance (Fig. 5d), the FNO/rGO//ACs LIC shows specific capacitances of 61 F g^{-1} (at 1 A g^{-1}) and 38.2 F g^{-1} (at 20 A g^{-1}), suggesting excellent rate capability.

The Ragone plot of the FNO/rGO//ACs LIC is presented in Fig. 5e. The energy and power density values were calculated according to eqn (4) and (5). Notably, the assembled LIC exhibits a maximum energy density of 135.6 W h kg^{-1} at a power density of 2000 W kg^{-1}, which is much higher than those of Ti- and Nb-based LICs reported previously, such as Nb_2O_5 nanorod film//AC,[26] $TiNb_2O_7$/HG//AC,[31] nitrogen-doped T-Nb_2O_5/tubular carbon (N–NbOC)//AC,[44] Nb_2O_5@carbon/reduced graphene oxide (M-Nb_2O_5@C/rGO)//AC,[45] and HG-$TiNb_{24}O_{62}$//carbon nanosheets.[46] Such outstanding energy and power densities are credited to the wide potential window from 0.01 to 4 V and excellent Li storage performance of the FNO/rGO active materials. Moreover, the results show good cycling stability of the FNO/rGO//ACs LIC, with capacitance retention of 88.5% after 5000 cycles at a charge/discharge current density of 2 A g^{-1} (Fig. 5f). The superior electrochemical performances of the FNO/rGO//ACs LIC may be due to the following factors: (1) graphene as a conducting medium makes FNO obtain more electrochemically active sites, thus enhancing the ion and electron transport kinetics; (2) the unique structure of FNO with interconnected three-dimensional channels and low-energy-barrier migration positions are beneficial to the transport and diffusion of Li^+; (3) the synergetic effect between graphene and FNO enhances the electrochemical performance; (4) the as-prepared FNO/rGO electrode exhibits an obvious pseudocapacitive behavior for Li storage, thus improving the anode kinetics; and (5) the wide potential window (0.01–3 V) of FNO/rGO could help to expand the working potential of LICs, resulting in high energy density. The aforementioned results demonstrate that the FNO/rGO composite is a very promising electrode material for LICs because of its excellent electrochemical performance.

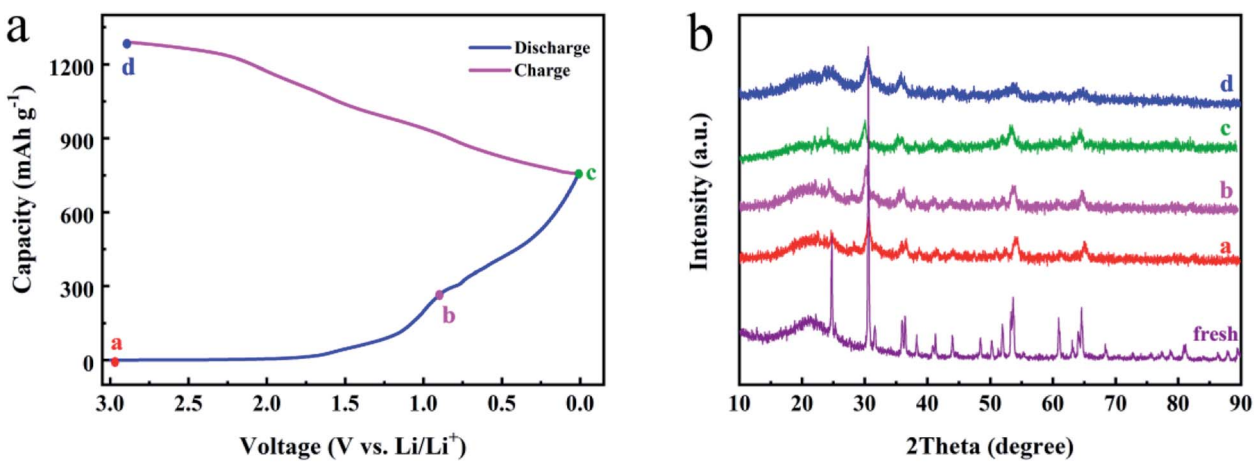

Fig. 4 The energy storage mechanism of FNO electrode. (a) The charge/discharge curve of FNO at the first cycle. (b) The corresponding *ex situ* XRD patterns.

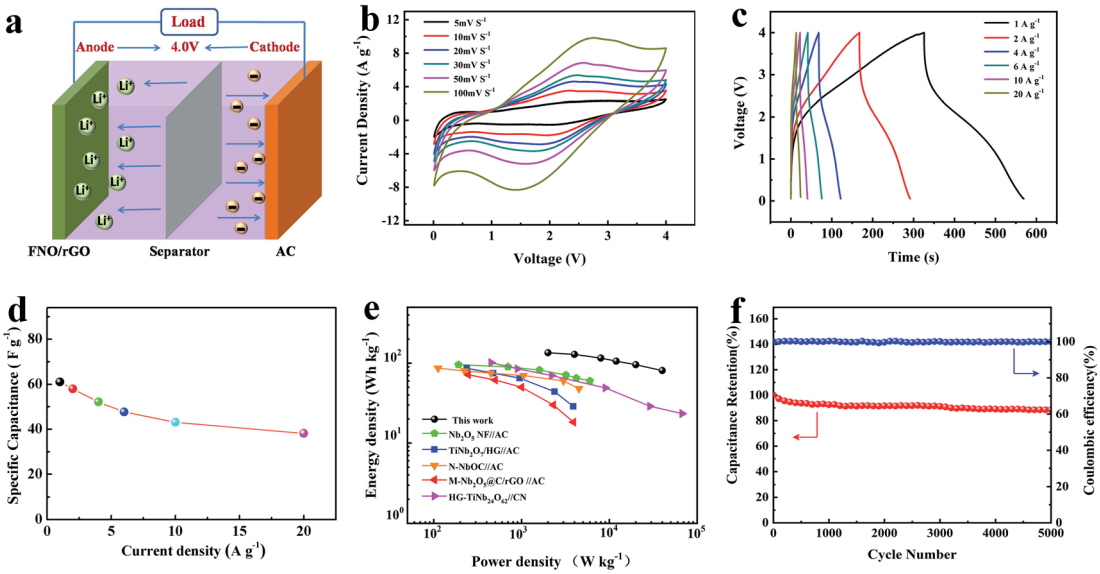

Fig. 5 Electrochemical performance of the FNO/rGO//AC LIC. (a) Schematic of the FNO/rGO//AC LIC configuration. (b) CV curves recorded at various scan rates. (c) GCD curves recorded at different current densities in the potential range 0.01–4.0 V. (d) Specific capacitance at various current densities. (e) Ragone plots. (f) Cycling performance at a current density of 2 A g^{-1}.

4 Conclusions

In summary, we have successfully designed an FNO/rGO hydrous electrode *via* a two-step hydrothermal method. The synergetic combination of graphene with high electronic conductivity and the unique structure of FNO promotes electrochemical reaction kinetics, shortens pathways for Li^+ diffusion, and reduces the volume change during the charge/discharge processes, which further results in excellent electrochemical performance. The FNO/rGO hybrid electrode exhibited a high reversible capacity (770 mA h g^{-1} at 0.05 A g^{-1}) and outstanding long-term cyclic stability (95.3% capacitance retention after 500 cycles). Furthermore, the FNO/rGO//ACs LIC achieved a high energy density of 135.6 W h kg^{-1} (at 2000 W kg^{-1}) and high rate capability (capacity retention of 63% from 1 to 20 A g^{-1}) with remarkable cycling performance (88.5% capacitance retention after 5000 cycles). This design of high-energy/high-power LIC is especially well-suited for developing next-generation energy storage systems.

Conflicts of interest

There are no conflicts to declare.

Acknowledgements

We gratefully acknowledge the financial support of this research by the Hong Kong Scholars Programs (grant no. XJ2016046), the Heilongjiang Postdoctoral Fund (LBHZ14054, LBH-TZ0609), the Natural Science Foundation Project of Chongqing Science and Technology Commission (no. cstc2019jcyj-msxmX0738), the Science and Technology Research Project of Chongqing Education Commission (KJQN201901411) and the Chongqing Municipal Education Commission (CXQT20026).

References

1 A. Noori, M. F. El-Kady, M. S. Rahmanifar, R. B. Kaner and M. F. Mousavi, Towards establishing standard performance metrics for batteries, supercapacitors and beyond, *Chem. Soc. Rev.*, 2019, **48**, 1272–1341.
2 J. Liu, J. Wang, C. Xu, H. Jiang, C. Li, L. Zhang, J. Lin and Z. X. Shen, Advanced energy storage devices: basic principles, analytical methods, and rational materials design, *Adv. Sci.*, 2018, **5**, 1700322.
3 H. Liu, X. Liu, S. Wang, H. K. Liu and L. Li, Transition metal based battery-type electrodes in hybrid supercapacitors: A review, *Energy Storage Mater.*, 2020, **28**, 122–145.
4 T. Kim and W. Song, Lithium-ion batteries: outlook on present, future, and hybridized technologies, *J. Mater. Chem. A*, 2019, **7**, 2942–2964.
5 F. Wu, J. Maier and Y. Yu, Guidelines and trends for next-generation rechargeable lithium and lithium-ion batteries, *Chem. Soc. Rev.*, 2020, **49**, 1569–1614.
6 L. Jin, C. Shen, A. Shellikeri, Q. Wu, J. Zheng, P. Andrei, J. G. Zhang and J. P. Zheng, Progress and perspectives on pre-lithiation technologies for lithium ion capacitors, *Energy Environ. Sci.*, 2020, **13**, 2341–2362.
7 D. Jia, W. Hu, E. Paek and D. Mitlin, Review of hybrid ion capacitors: From aqueous to lithium to sodium, *Chem. Rev.*, 2018, **118**, 6457–6498.
8 F. Yu, T. Huang and P. P. Zhang, Design and synthesis of electrode materials with both battery-type and capacitive charge storage, *Energy Storage Mater.*, 2019, **22**, 235–255.
9 Y. Wu, C. Li, W. Wu, S. Zhang, L. He, Y. Zhu, J. Wang, L. Fu, Y. Chen and W. Huang, A high-voltage aqueous lithium ion

capacitor with high energy density from an alkaline-neutral electrolyte, *J. Mater. Chem. A*, 2019, **7**, 4110–4118.

10 P. X. Han, G. J. Xu, X. Q. Han, J. W. Zhao, X. H. Zhou and G. L. Cui, Lithium ion capacitors in organic electrolyte system: scientific problems, material development, and key technologies, *Adv. Energy Mater.*, 2018, **8**, 1801243.

11 Y. L. Zhang, H. X. Chao and H. Y. Liu, Regulation of the cathode for amphi-charge storage in a redox electrolyte for high-energy lithium-ion capacitors, *Chem. Commun.*, 2020, **56**, 12777–12780.

12 L. Kouchachvili, W. Yaici and E. Entchev, Hybrid battery/supercapacitor energy storage system for the electric vehicles, *J. Power Sources*, 2018, **374**, 237–248.

13 M. V. Reddy, G. V. S. Rao and B. V. R. Chowdari, Metal oxides and oxysalts as anode materials for Li ion batteries, *Chem. Rev.*, 2013, **113**, 5364–5457.

14 I. Rabani, J. Yoo, H. S. Kim, D. V. Lam, S. Hussain, K. Karuppasamy and Y. S. Seo, Highly dispersive Co_3O_4 nanoparticles incorporated in a cellulose nanofiber for a high-performance flexible supercapacitor, *Nanoscale*, 2021, **13**, 355–370.

15 K. Karuppasamy, D. Vikraman, J. H. Choi, R. Bose, A. Nichelson, T. Maiyalagan and H. S. Kim, Hybrid lithium-ion capacitors based on novel 1-butyl-3-methylimidazolium bis(nonafluorobutanesulfonyl imide) (BMImBNFSI) ionic liquid electrolytes: a detailed investigation of electrochemical and cycling behaviors, *J. Mater. Res. Technol.*, 2020, **9**, 5216–5227.

16 D. Vikraman, S. Hussain, K. Karuppasamy, A. Feroze, A. Kathalingam, A. Sanmugam, S. H. Chun, J. Jung and H. S. Kim, Engineering the novel $MoSe_2$-Mo_2C hybrid nanoarray electrodes for energy storage and water splitting applications, *Appl. Catal., B*, 2020, **264**, 118531.

17 K. Karuppasamy, D. Vikraman, I. T. Hwang, H. J. Kim, A. Nichelson, R. Bose and H. S. Kim, Nonaqueous liquid electrolytes based on novel 1-ethyl-3-methylimidazolium bis (nonafluorobutane-1-sulfonyl imidate) ionic liquid for energy storage devices, *J. Mater. Res. Technol.*, 2020, **9**, 1251–1260.

18 G. J. Xu, P. X. Han, S. M. Dong, H. S. Liu, G. L. Cui and L. Q. Chen, $Li_4Ti_5O_{12}$-based energy conversion and storage systems: Status and prospects, *Coord. Chem. Rev.*, 2017, **343**, 139–184.

19 J. H. Huo, Y. J. Xue and X. F. Wang, TiO_2/carbon nanofibers doped with phosphorus as anodes for hybrid Li-ion capacitors, *J. Power Sources*, 2020, **473**, 228551.

20 M. Li, Y. Yang, E. S. G. Choo, X. Tang, K. Sun, Y. Chen and J. Xue, TiO_2-B nanofibrils reinforced graphene paper for multifunctional flexible electrode, *J. Power Sources*, 2018, **394**, 131–139.

21 J. Q. Liao, W. Ni and C. Y. Wang, Layer-structured niobium oxides and their analogues for advanced hybrid capacitors, *Chem. Eng. J.*, 2020, **391**, 123489.

22 B. Deng, H. Dong, T. Lei, N. Yue, L. Xiao and J. Liu, Post-annealing tailored 3D cross-linked $TiNb_2O_7$ nanorod electrode: towards superior lithium storage for flexible lithium-ion capacitors, *Sci. China Mater.*, 2020, **63**, 492–504.

23 S. Hemmati, G. Li, X. L. Wang, Y. L. Ding, Y. Pei, A. P. Yu and Z. W. Chen, 3D N-doped hybrid architectures assembled from 0D T-Nb_2O_5 embedded in carbon microtubes toward high-rate Li-ion capacitors, *Nano Energy*, 2019, **56**, 118–126.

24 Z. J. Chen, H. S. Li, L. Y. Wu, X. X. Lu and X. G. Zhang, $Li_4Ti_5O_{12}$ Anode: structural design from material to electrode and the construction of energy storage devices, *Chem. Rec.*, 2018, **18**, 350–380.

25 Q. Deng, Y. Fu, C. Zhu and Y. Yu, Niobium-based oxides toward advanced electrochemical energy storage: recent advances and challenges, *Small*, 2019, 1804884.

26 B. H. Deng, T. Y. Lei, W. H. Zhu, L. Xiao and J. P. Liu, In-plane assembled oorthorhombic Nb_2O_5 nanorod films with high-rate Li^+ intercalation for high-performance flexible Li-ion capacitors, *Adv. Funct. Mater.*, 2018, **28**, 1704330.

27 J. Wu, G. Pan, W. Zhong, L. Yang, S. Deng and X. Xia, Rational synthesis of $Cr_{0.5}Nb_{24.5}O_{62}$ microspheres as high-rate electrodes for lithium ion batteries, *J. Colloid Interface Sci.*, 2020, **562**, 511–517.

28 L. Yan, H. Lan, H. Yu, S. Qian, X. Cheng, N. Long, R. Zhang, M. Shui and J. Shu, Electrospun $WNb_{12}O_{33}$ nanowires: superior lithium storage capability and their working mechanism, *J. Mater. Chem. A*, 2017, **5**, 8972–8980.

29 Q. Fu, J. Hou, R. Lu, C. Lin, Y. Ma, J. Li and Y. Chen, Electrospun $Ti_2Nb_{10}O_{29}$ hollow nanofibers as high-performance anode materials for lithium-ion batteries, *Mater. Lett.*, 2018, **214**, 60–63.

30 H. Zhu, L. Yan, M. Xia, X. Cheng, W. Ye, H. Yu, N. Long, M. Shui and J. Shu, Controlledformation of BNb_3O_9 nanobelts as superior host material for high performance electrochemical energy storage, *J. Power Sources*, 2019, **426**, 250–258.

31 X. Y. Jiao, Q. L. Hao, X. F. Xia, D. Yao, Y. Ouyang and W. Lei, Boosting long-cycle-life energy storage with holey graphene supported $TiNb_2O_7$ network nanostructure for lithium ion hybrid supercapacitors, *J. Power Sources*, 2018, **403**, 66–75.

32 S. Y. Kong, K. Cheng, T. Ouyang, Y. Y. Gao, K. Ye, G. L. Wang and D. X. Cao, Facile electrodepositing processed of RuO_2-graphene nanosheets-CNT composites as a binder-free electrode for electrochemical supercapacitors, *Electrochim. Acta*, 2017, **246**, 433–442.

33 S. Y. Kong, K. Cheng, Y. Y. Gao, T. Ouyang, K. Ye, G. L. Wang and D. X. Cao, A novel three-dimensional manganese dioxide electrode for high performance supercapacitors, *J. Power Sources*, 2016, **308**, 141–148.

34 X. Zhang, J. Y. Zhang, S. Y. Kong, K. Zhu, J. Yan, K. Ye, G. L. Wang, K. Cheng, L. M. Zhou and D. X. Cao, A novel calendula-like $MnNb_2O_6$ anchored on graphene sheet as high-performance intercalation pseudocapacitive anode for lithium-ion capacitors, *J. Mater. Chem. A*, 2019, **7**, 2855–2863.

35 Y. Z. Jiao, H. T. Zhang, H. L. Zhang, A. Liu, Y. X. Liu and S. J. Zhang, Highly bonded T-Nb_2O_5/rGO nanohybrids for 4 V quasi-solid state asymmetric supercapacitors with improved electrochemical performance, *Nano Res.*, 2018, **11**, 4673–4685.

36 E. Husson, Y. Repelin, N. Q. Dao and H. Brusset, Normal coordinate analysis of MNb_2O_6 series of columbite

structure (M=Mg, Ca, Mn, Fe, Co, Ni, Cu, Zn, Cd), *J. Chem. Phys.*, 1977, **67**, 1157–1163.

37 F. X. Huang, Q. Zhou, L. Li, X. L. Huang, D. P. Xu, F. F. Li and T. Cui, Structural Transition of $MnNb_2O_6$ under Quasi-Hydrostatic Pressure, *J. Phys. Chem. C*, 2014, **118**, 19280–19286.

38 E. Husson, Y. Repelin, N. Q. Dao and H. Brusset, Normal coordinate analysis for $CaNb_2O_6$ of columbite structure, *J. Chem. Phys.*, 1977, **66**, 5173–5180.

39 R. Z. Li, Y. M. Wang, C. Zhou, C. Wang, X. Ba, Y. Y. Li, X. T. Huang and J. P. Liu, Carbon-stabilized high-capacity ferroferric oxide nanorod array for flexible solid-state alkaline battery-supercapacitor hybrid device with high environmental suitability, *Adv. Funct. Mater.*, 2015, **25**, 5384–5394.

40 C. Yang, Y. L. Zhang, F. Lv, C. F. Lin, Y. Liu, K. Wang, J. R. Feng, X. H. Wang, Y. J. Chen, J. B. Li and S. J. Guo, Porous $ZrNb_{24}O_{62}$ nanowires with pseudocapacitive behavior achieve high-performance lithium-ion storage, *J. Mater. Chem. A*, 2017, **5**, 22297–22304.

41 L. F. Shen, H. F. Lv, S. Q. Chen, P. Kopold, P. A. van Aken, X. J. Wu, J. Maier and Y. Yu, Peapod-like Li_3VO_4/N-doped carbon nanowires with pseudocapacitive properties as advanced materials for high-energy lithium-ion capacitors, *Adv. Mater.*, 2017, **29**, 1700142.

42 W. W. Liu, J. D. Li, K. Feng, A. Sy, Y. S. Liu, L. Lim, G. Lui, R. Tjandra, L. Rasenthiram, G. Chiu and A. P. Yu, Advanced Li-ion hybrid supercapacitors based on 3D graphene-foam composites, *ACS Appl. Mater. Interfaces*, 2016, **8**, 25941–25953.

43 V. Augustyn, J. Come, M. A. Lowe, J. W. Kim, P. L. Taberna, S. H. Tolbert, H. D. Abruna, P. Simon and B. Dunn, High-rate electrochemical energy storage through Li^+ intercalation pseudocapacitance, *Nat. Mater.*, 2013, **12**, 518–522.

44 S. Hemmati, G. Li, X. L. Wang, Y. L. Ding, Y. Pei, A. P. Yu and Z. W. Chen, 0 D T-Nb_2O_5 embedded in carbon microtubes toward high-rate Li-ion capacitors, *Nano Energy*, 2019, **56**, 118–126.

45 X. Jiao, Q. Hao, X. Xia, Z. Wu and W. Lei, Metal organic framework derived Nb_2O_5@C nanoparticles grown on reduced graphene oxide for high-energy lithium ion capacitors, *Chem. Commun.*, 2019, **55**, 2692–2695.

46 S. H. Li, J. W. Chen, X. F. Gong, J. X. Wang and P. S. Lee, Holey graphene-wrapped porous $TiNb_{24}O_{62}$ microparticles as high-performance intercalation pseudocapacitive anode materials for lithium-ion capacitors, *NPG Asia Mater.*, 2018, **10**, 406–416.